

Shoreward shift of oceanic mesoscale activity over the last three decades

Received: 14 August 2024

Accepted: 14 October 2025

Published online: 24 November 2025

Shuyi Zhou^{1,5}, Yihang Zhang^{1,5}, Hong Li², Lingxiao Liu³, Enhui Liao⁴ & Fanghua Xu¹✉

Oceanic mesoscale activity critically mediates the cross-shelf exchange of heat, nutrients, carbon, and pollutants. While its meridional shifts under global warming are well studied, zonal migration remains unknown. Here, based on multi-source observation and reanalysis datasets, we find that zonal centroids of both global mesoscale eddy kinetic energy (EKE) and global sea surface temperature gradient magnitudes have shifted shoreward at approximately 35.4 ± 22.5 and 34.4 ± 20.3 km per decade respectively over the last three decades (1993–2022). Energy budget analysis indicated that a shoreward shift of wind power and baroclinic energy conversion under global warming primarily has occurred in parallel with the EKE onshore migration. These shifts are reshaping coastal–open ocean exchanges, and thereby are essential for predicting coastal ecosystem resilience under climate change.

Oceanic mesoscale activity, characterized by horizontal scales ranging from tens to hundreds of kilometers, accounts for almost 90% of the global ocean kinetic energy¹, serving as principal regulators in the global energy budget and biogeochemical cycling^{2–4}. In coastal transition zones, mesoscale fronts and eddies act as critical interfacial mediators, facilitating cross-shelf transport of momentum, heat, dissolved carbon, nutrients, and pollutants^{1,5–12}. These processes exert cascading effects on environments and ecosystems¹³, as well as resource sustainability^{14,15} in coastal regions. Rapid ocean warming observed over the past few decades¹⁶, however, can alter these fundamental processes. Therefore, elucidating the zonal evolution of global mesoscale activity under global warming emerges as a scientific imperative for refining climate prediction, advancing sustainable ocean governance frameworks, and informing evidence-based coastal adaptation strategies.

Recent studies have investigated changes in global oceanic mesoscale activity via observations, reanalysis, and numerical simulation, but mainly focused on the meridional^{15,17–24}. The poleward shift of oceanic mesoscale activity in the western boundary currents of the Southern Hemisphere^{15,19}, as well as the increase of mesoscale activity near both poles are observed^{20,23,24}. Based on eddy kinetic energy (EKE)

and sea surface temperature gradient magnitudes ($|\nabla SST|$), J. Martínez-Moreno et al.¹⁸ found that oceanic mesoscale eddies in eddy-rich regions, such as the western boundary currents and their extensions, have exhibited increased variability over the past several decades. From long-term observations, Beal and Elipot²⁵ found that the increased mesoscale activity broadens the Agulhas Current via enhanced lateral viscous effects. Furthermore, recent observation²⁵ and numerical²⁶ studies indicated that the western boundary currents migrated shoreward over the past decades, implying a possible shoreward shift of oceanic mesoscale activity. However, little is known about the zonal evolution of mesoscale activity in global oceans under current and future warming.

To investigate the zonal evolution of ocean mesoscale activity, we examine EKE and $|\nabla SST|$ from multiple data sources (see “Methods” for details), including one eddy-resolving reanalysis product (GLORYS), one eddy-resolving ocean hindcast (OFES), three satellite-derived datasets (AVISO, CMEMS and OISST), as well as two eddy-resolving climate models (FGOALS and HadGEM3) from Climate Model Inter-comparison Project phase 6²⁷ (CMIP6) models. A tracer-weighted average operator is applied to quantify the zonal distribution of EKE and $|\nabla SST|$, named as “zonal centroid” (enlightened by Yang et al.²⁸,

¹Department of Earth System Science, Ministry of Education Key Laboratory for Earth System Modeling, Institute for Global Change Studies, Tsinghua University, Beijing, China. ²Tianjin Key Laboratory for Marine Environmental Research and Service, School of Marine Science and Technology, Tianjin University, Tianjin, China. ³Intelligent Forecasting Division, Ninecosmos Science and Technology Ltd., Wuxi, China. ⁴School of Oceanography, Shanghai Jiao Tong University, Shanghai, China. ⁵These authors contributed equally: Shuyi Zhou, Yihang Zhang. ✉e-mail: fxu@tsinghua.edu.cn

see “Methods” for details). The zonal centroids of EKE and $|\nabla SST|$ are then calculated for 10 key regions²⁹, including five western regions and five eastern regions (Fig. 1a and Table S1). The shift trends of zonal centroids are obtained by linear regression, and the significance is tested via the Student’s *t*-test. Significant shoreward intensification of oceanic mesoscale activity is found in most of the regions. The energy analysis reveals that both surface wind power and baroclinic energy conversion have also shifted onshore. Furthermore, we compute the zonal centroids of EKE and $|\nabla SST|$ under the high-emission RCP8.5 scenario (2015–2050) from CMIP6 models to discuss the zonal evolution of oceanic mesoscale activity in response to global warming.

Results

Shoreward shift of oceanic mesoscale activity in past decades

Figure 1a shows the global trends of sea surface EKE from 1993 to 2022, derived from GLORYS. In the western boundary current regions, the EKE shows increased trends in the polar flank and decreased trends in the equatorial flank, implying the poleward shifts of EKE, consistent with previous studies^{15,17,19,28,30,31}. In terms of the zonal distribution, the trend of EKE generally increases near the coasts, such as the China marginal seas, the California coast, and so on. Except for the western South Atlantic (WSA), all regions exhibit shoreward intensification of

EKE (Fig. 1b–k). The global averaged zonal shift speed of sea surface EKE from GLORYS is 41.7 ± 14.4 km per decade (Fig. 1l). Notably, we select a wide region from the coast to the middle of the open ocean to calculate the zonal centroids of EKE. In this way, the overall changes in mesoscale activity distribution across the ocean basin over the recent three decades are quantified. To reveal changes of mesoscale activity from near-shelf to coast, we also select the nearshore region and calculate the shifts of the associated zonal centroids (Fig. S1). The shoreward shifts of EKE appear in most of the nearshore regions, consistent with the results obtained from the large domain (Fig. 1).

$|\nabla SST|$, a well-established proxy for oceanic mesoscale activity, also exhibit pronounced onshore intensification patterns. As shown in Fig. 2 and Fig. S2, the 1993–2022 period shows marked amplification of $|\nabla SST|$ signatures within coastal regions. This spatial coherence aligns with observed asymmetries in regional SST warming, i.e., faster warming is observed near the coasts compared to adjacent open oceans (Fig. S3). The concurrent intensification of nearshore $|\nabla SST|$ (Fig. 2a) and EKE centroid migration (Fig. 1a) suggests both momentum and temperature processes drive the coastal mesoscale activity over the recent three decades.

Additionally, Figs. 1a and 2a show that approximately 40% and 30% of the grid points exhibit significant local trends in EKE and $|\nabla SST|$, respectively. However, these significant temporal trends in

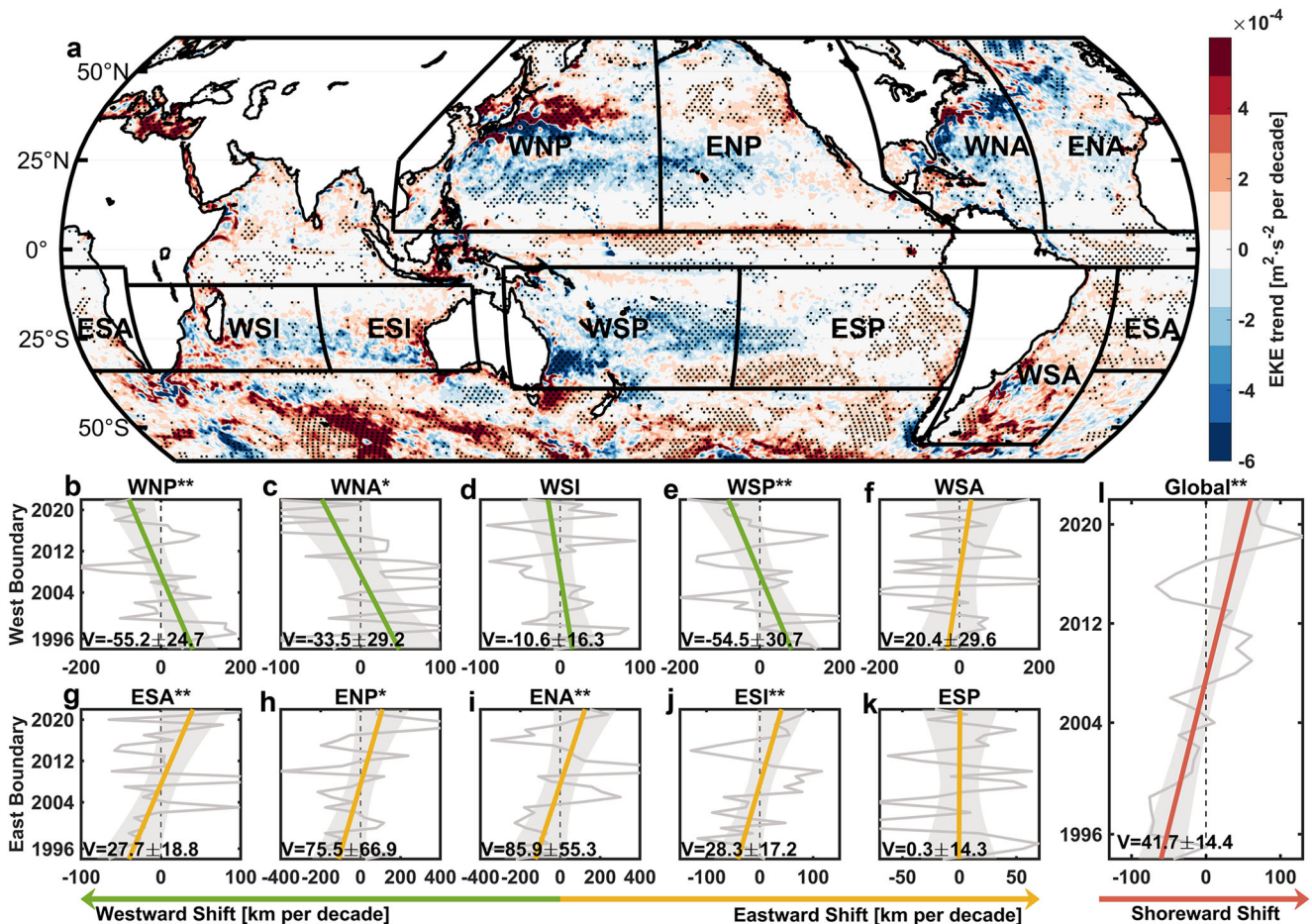


Fig. 1 | Global trends of sea surface eddy kinetic energy (EKE) and their zonal centroid shifts from 1993 to 2022 from GLORYS. a Distribution of surface EKE trends. **b–k** Time-series of zonal centroid anomalies (compared to the mean location over the time period) of EKE (gray) in west boundary regions including Western North Pacific (WNP, **b**), Western North Atlantic (WNA, **c**), Western South Indian Ocean (WSI, **d**), Western South Pacific (WSP, **e**) and Western South Atlantic (WSA, **f**), east boundary regions including Eastern South Atlantic (ESA, **g**), Eastern

North Pacific (ENP, **h**), Eastern North Atlantic (ENA, **i**), Eastern South Indian Ocean (ESI, **j**), and Eastern South Pacific (ESP, **k**), and the global ocean **l**, superimposed with the linear trends. Gray shadings are the 95% confidence intervals for the linear fit based on the Student’s *t*-test. The plot labeled with * and ** indicates significance at the 90% and 95% confidence level, respectively. “V = ” on subplots “b–l” describes the shift speed in km per decade. The black dots indicate regions where the EKE trends are significant at 90%.

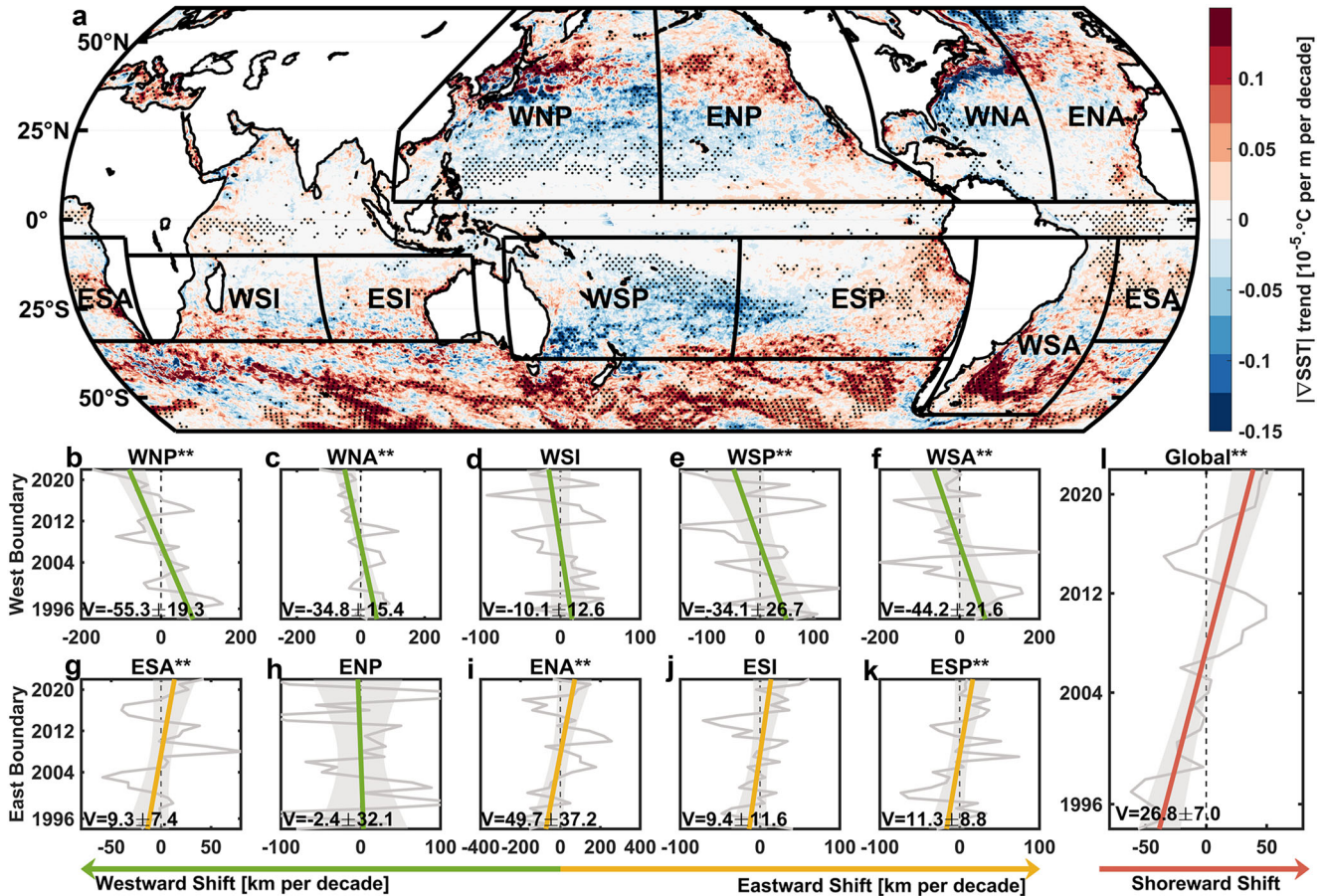


Fig. 2 | Global trends of global sea surface temperature gradient magnitude ($|\text{VSST}|$) and their zonal centroid shifts from 1993 to 2022 from GLORYS.
a Distribution of global $|\text{VSST}|$ trends. **b–k** Time-series of zonal centroid anomalies (compared to the mean location over the time period) of $|\text{VSST}|$ (gray) in west boundary regions (**b–f**), east boundary regions (**g–k**), and the global ocean.

l Superimposed with the linear trends. Gray shadings are the 95% confidence intervals for the linear fit based on the Student's t -test. The figure labeled with * and ** indicates significance at the 90% and 95% confidence level, respectively. “ V = ” on subplots “**b–l**” describes the shift speed in km per decade. The black dots indicate regions where the $|\text{VSST}|$ trends are significant at 90%.

EKE and $|\text{VSST}|$ are distinct from the significance of the zonal centroid shifts. The former are local metrics, while the latter evaluates large-scale spatial redistribution. Consequently, the local trends cannot be used to directly determine the significance of changes in the zonal centroids.

Coherent shoreward shift of zonal centroids of EKE and $|\text{VSST}|$ appears in the global average across all observational, reanalysis and model hindcast products (Fig. 3a, b), with a multi-dataset mean displacement rate of 35.4 ± 22.5 km per decade and 34.4 ± 20.3 km per decade over the past three decades, respectively. Notably, reanalysis systems (GLORYS), model hindcast (OFES) and satellite-derived datasets demonstrate convergent trends (~ 35 km per decade).

Regionally, western basin regions exhibit robust patterns, showing statistically significant EKE/ $|\text{VSST}|$ centroid shoreward shifts in the analysis (Fig. 3a, b). For EKE, the WNA, WNP, WSP, and WSI regions demonstrate cross-dataset consistency, whereas the WSA region presents paradoxical behavior, its zonal EKE centroid demonstrates an offshore displacement in all datasets except CMEMS. The offshore shift in WSA is potentially linked to South Atlantic SST front intensification and Brazil Current frontal variability^{32,33}. For $|\text{VSST}|$, shoreward shifts appear in all regions and all datasets, except OFES in the WNA.

Eastern basin regions display greater dynamical complexity. The zonal centroids of EKE [in all regions display shoreward shift trends in most of the datasets (Fig. 3a), while $|\text{VSST}|$ exhibits inter-dataset spread (Fig. 3b). The results from GLORYS and OFES are not all consistent with those from OISST, likely reflecting deficiencies in models. The offshore

trends of $|\text{VSST}|$ in the eastern basin regions primarily resulted from the enhancement of SST in open oceans, evident in SST trends (Fig. S3). In contrast, the shoreward trends of $|\text{VSST}|$ in OISST are apparent in the nearshore regions (Fig. S2), consistent with the same regional significant shoreward EKE centroid shifts (Fig. S1).

Overall, there is a consistent shoreward shift of the zonal centroids of EKE and $|\text{VSST}|$ in approximately 77% regions, suggesting the redistribution of oceanic mesoscale activities over the past several decades. Observations from satellite observations are generally consistent with the results of GLORYS reanalysis, as well as the model hindcast (OFES).

Primary drivers

To investigate the potential dynamics driving the shoreward shift of the oceanic mesoscale activity over the past three decades, we analyze global trends of primary EKE source terms, including surface wind power (WP), baroclinic energy conversion (BC), and barotropic energy conversion (BT), derived from GLORYS^{34,35} (see “Methods” for details). The trend of these terms is spatially heterogeneous and obvious near the shore (Fig. 4a, c, e), implying the drastic changes of EKE over the recent decades. Note that surface wind power primarily acts as eddy-killing effects in regions with strong currents, while the wind work can be positive in coastal regions where the winds can drive small-scale currents^{36,37}. The global mean distribution of WP³⁸ shows that the mean WP is primarily negative along major ocean currents, while positive near the coasts. The zonal centroids of these energy terms are

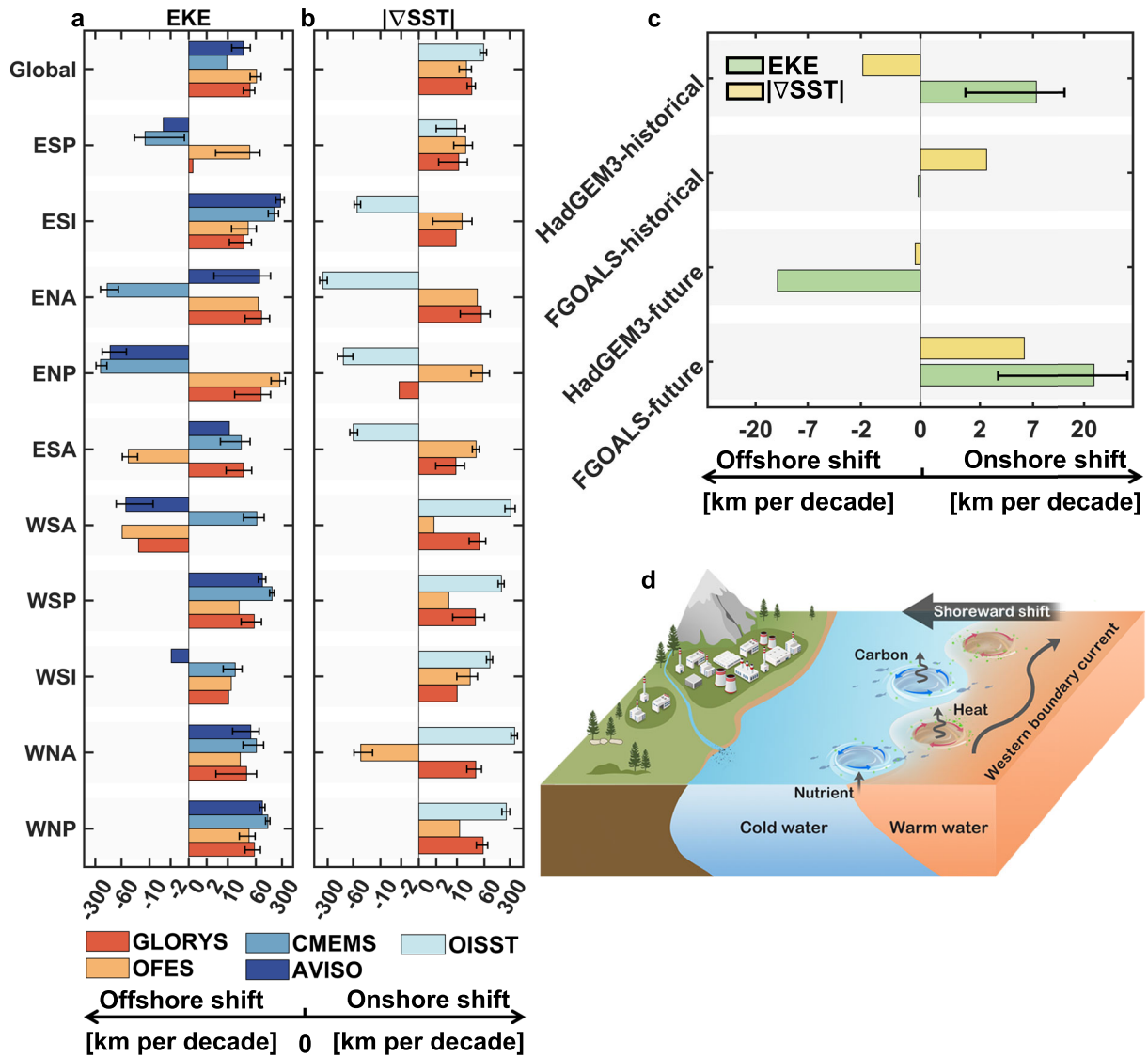


Fig. 3 | Summary of the shift trends of the zonal centroids of oceanic mesoscale activity. **a, b** Values of the shift trends of eddy kinetic energy (EKE) and sea surface temperature gradient magnitude ($|\nabla SST|$) zonal centroids in different datasets. **c** Values of the shift trends of EKE and $|\nabla SST|$ zonal centroids from CMIP6

HighResMIP historical and future experiments. **d** Schematic diagram of the shoreward shift of mesoscale activity, taking the western boundary current region as an example. Error bars are shown only for trends statistically significant at the 90% confidence level or higher.

calculated to provide an integrated metric for evaluating whether the net energy forcing is shifting onshore. Since these energy terms contribute to the temporal evolution of EKE, the qualitative direction of these centroid movements indicates an onshore or offshore shifting in energy forcing. Figure 4b, d demonstrate significant shoreward shifts in the zonal centroids of WP (0.36 ± 0.28 km per decade) and BC (0.07 ± 0.04 km per decade), whereas the zonal centroid of BT (0.21 ± 0.32 km per decade) exhibits an insignificant offshore trend (Fig. 4f). The shifting directions of WP and BC are consistent with that of oceanic mesoscale activity, suggesting both WP and BC contribute to the onshore migration of EKE. Furthermore, the spatial trend distribution of the shoreward shift of WP is more consistent with that of EKE and $|\nabla SST|$, implying that the WP is more responsible for the onshore shift of mesoscale activity.

The shoreward shift of WP is primarily attributed to intensified wind stress near coastal boundaries (Fig. S4). One possibility for intensified wind stress near coastal boundaries is amplified land-ocean thermal contrast under global warming³⁵. The shoreward shift of BC may be associated with enhanced open-ocean stratification, primarily

induced by temperature changes under global warming in the subtropics and mid-latitudes^{39,40}. Zonal variations in mesoscale activity may also be linked to the shoreward shift of the western boundary currents^{25,26,41}.

Furthermore, the increased nearshore $|\nabla SST|$ may also be linked to the intensification of alongshore winds. According to the established hypothesis of Bukun⁴², intensified alongshore winds enhance upwelling in eastern boundary current systems, which inhibits nearshore SST rise and amplifies the cross-shelf gradient. In western boundary regions, which lack major upwelling systems, intensified alongshore winds may enhance mixing in the upper ocean, thereby suppressing the SST increasing rate and also strengthening the SST gradient. Concurrently, the enhanced stirring of mesoscale processes can also increase the nearshore SST gradient. Additionally, under global warming, enhanced ocean stratification can lead to onshore intensification of western boundary currents³⁹, and thereby contribute to the $|\nabla SST|$ shoreward shift. A more targeted analysis is required to quantitatively disentangle the relative contributions of these mechanisms to this trend.

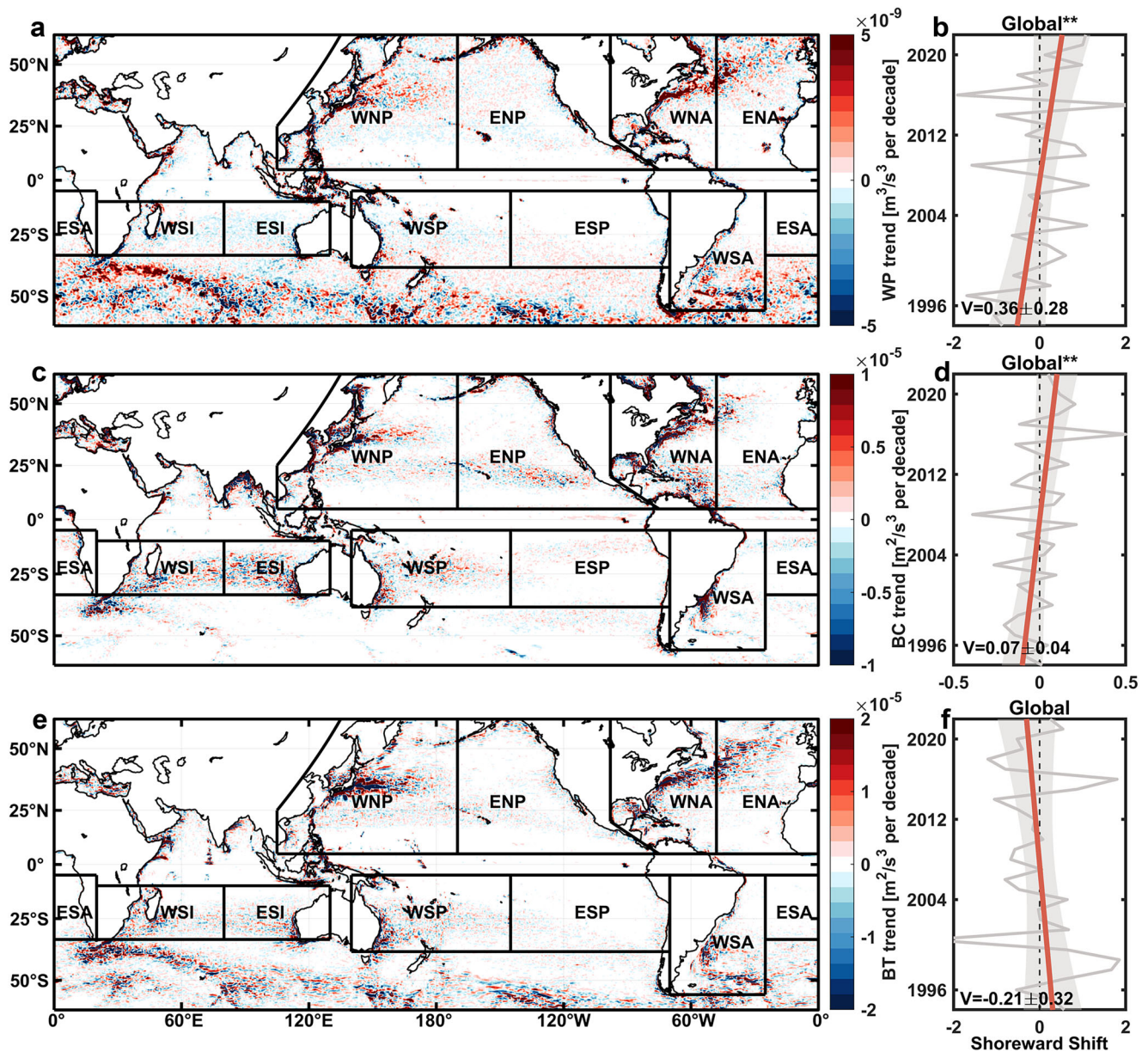


Fig. 4 | Surface wind power and baroclinic instability contribute dominantly to the shoreward shifts of mesoscale activity. a, c, e Global trends of surface wind power (WP), baroclinic instability (BC), and barotropic instability (BT) from 1993 to

2022 calculated using GLORYS. **b, d, f** Global-averaged time-series of zonal centroid anomalies (compared to the mean location over the time period) of WP, BC, and BT, respectively [Unit: km per decade].

Implications from high-resolution CMIP6 projections

To investigate zonal shift trends of oceanic mesoscale activity under global warming, we analyze two high-resolution simulations (HadGEM3 and FGOALS) from the CMIP6 HighResMIP future experiments under the RCP8.5 scenario (from 2015 to 2050). RCP8.5, representing the worst-case climate pathway in IPCC projections, projects 4.3–4.8°C global warming by 2100 under unabated fossil fuel dependence.

HadGEM3 and FGOALS exhibit divergent zonal shift trends for EKE and $|\nabla SST|$ (Fig. 3c). HadGEM3-historical simulates a significant shoreward EKE displacement, while FGOALS-historical shows an insignificant offshore trend. Although the future shift trend of EKE zonal centroid aligns with that of $|\nabla SST|$, the inter-model discrepancy reveals substantial uncertainties in projecting future mesoscale activity. These uncertainties emphasize the need to prioritize coastal monitoring. Furthermore, accurately simulating the zonal shift of mesoscale activities is critical for reducing air-sea flux biases and

improving ocean circulation representation, an ongoing challenge for climate model development. Our findings provide a quantitative metric for evaluating eddy-resolving climate models.

Discussion

Our analysis reveals a consistent shoreward shift of sea surface EKE and $|\nabla SST|$ across multiple ocean basins under global warming. Multi-dataset synthesis indicates global-averaged shift speeds of 35.4 ± 22.5 (EKE) and 34.4 ± 20.3 ($|\nabla SST|$) km per decade with pronounced trends in the western basin regions (Fig. 3a, b). The shift speeds of EKE and $|\nabla SST|$ zonal centroids are spatially correlated, a plausible explanation being that the shoreward shift of nearshore $|\nabla SST|$ can increase the nearshore baroclinic instability, providing favorable conditions for the generation and maintenance of oceanic mesoscale activity.

EKE budget analysis reveals that both surface wind power and baroclinic energy conversion have also shifted onshore. Furthermore, the onshore intensification reported recently²⁶ may be related to the

shoreward shift of oceanic mesoscale activity. However, this phenomenon is not robust in CMIP6 models, likely due to insufficient horizontal resolution for resolving submesoscale and smaller-scale processes. Most of the CMIP6 simulations, with 0.25° horizontal resolution, are eddy-present⁴³. This resolution is still too coarse to study mesoscale activity, particularly near high latitudes where the Rossby radius is only tens of kilometers⁴⁴.

Here, we define “mesoscale activity” more comprehensively, using a high-pass filter to capture all mesoscale signals, which include but are not limited to eddies and fronts. The behavior of mesoscale eddies and fronts is a component of the overall signals; the extent to which their propagation changes accounts for the full zonal migration remains an open question worthy of further study.

The global warming-induced changes in oceanic mesoscale activity may alter coastal material exchange⁴⁵ (Fig. 3d). For example, prolonged advection routes may reduce offshore nutrient transport by eastern boundary eddies, exacerbating subtropical ocean “desertification.” The observed shoreward shift of |∇SST| zonal centroids may extend to subsurface layers, influencing deeper mesoscale dynamics. Eddy-driven subduction pumps nutrients vertically via ageostrophic secondary circulation^{46,47}, enhancing nearshore heat/carbon fluxes and biological productivity⁴⁸. Thus, reconfigured coastal-open ocean exchanges may disrupt nutrient distribution, with cascading impacts on fisheries and biodiversity. It is urgent to integrate mesoscale dynamics into climate adaptation strategies to mitigate ecological and socioeconomic risks.

Methods

Datasets

For satellite observations, we use the daily Optimum Interpolation SST (OISST) sea surface temperature data from the National Oceanic and Atmospheric Administration, sea water velocity from the daily Global Ocean Gridded L4 Sea Surface Heights And Derived Variables Nrt of the Copernicus Marine Environment Monitoring Service (CMEMS), and the monthly Archiving, Validation and Interpretation of Satellite Oceanographic data (AVISO), with 0.25° horizontal resolution.

For eddy-resolving reanalysis product and ocean model simulation, we use the daily sea water velocity and SST from Global Ocean Physics Reanalysis (GLORYS) of CMEMS (1/12° horizontal resolution) and the monthly Ocean General Circulation Model for the Earth Simulator (OFES) developed at the Japan Agency for Marine-Earth Science and Technology (0.1° horizontal resolution). GLORYS is widely used in the study of oceanic mesoscale dynamics and has been proven to do well in regions such as the NW Atlantic shelf⁴⁹. The time range of the above datasets is from 1993 to 2022.

For climate model simulations, we use the monthly sea water velocity and SST of the historical and future experiment from CMIP6 High Resolution Model Intercomparison Project (HighResMIP), including two models (10 km horizontal resolution), namely FGOALS-f3-H (FGOALS) and HadGEM3-GC31-HH (HadGEM3). Normally, the future experiment under the RCP 8.5 scenario and the historical experiment are on the 2015–2050 and 1950–2014 period, respectively. Due to the lack of data, however, only the historical experiments of HadGEM3 from 1955 to 2014 are obtained.

The wind stress data with 0.25° horizontal resolution is obtained directly from the monthly Ocean Reanalysis System 5 (ORASS) prepared by the European Center for Medium-Range Weather Forecasts (ECMWF) ocean analysis-reanalysis system.

Zonal centroid calculation

The zonal centroid defined in this study serves as a metric to quantify the overall distribution of oceanic mesoscale activity across the entire region. It is essentially the regional average of the λ-direction arc length relative to a certain reference longitude (for ESA it is 180° and for other regions it is 0°), which is weighted by the variable

field $F(\lambda, \varphi)$ and the spherical area element dS at (λ, φ) . The unweighted arc length at the location (λ, φ) relative to the reference longitude is:

$$lx(\lambda, \varphi) = (R \cos \varphi) \cdot \left(\lambda \frac{\pi}{180} \right) = \frac{\pi R}{180} \lambda \cos \varphi \quad (1)$$

dS at (λ, φ) is:

$$dS = (R d\varphi) \cdot (R \cos \varphi d\lambda) = R^2 \cos \varphi d\lambda d\varphi \quad (2)$$

Therefore, the average of the weighted arc length over the whole region, namely the zonal centroid, is:

$$\bar{x} = \frac{\iint lx \cdot F \cdot dS}{\iint F \cdot dS} = \frac{\pi R \iint \lambda F \cos^2 \varphi d\lambda d\varphi}{180 \iint F \cos \varphi d\lambda d\varphi} \quad (3)$$

where R is the radius of the Earth, R is 6371 km. λ and φ are longitude and latitude, respectively. $F = F(\lambda, \varphi)$ is the variable field under latitude-longitude coordinates. In this study, F can be the field of variables. $d\lambda$ and $d\varphi$ are the elements of λ and φ in the spherical coordinate, respectively. Herein, $d\lambda$ and $d\varphi$ are the horizontal spatial resolutions of F in the zonal and meridional directions, respectively.

The calculation proceeds as follows. We first calculate annual mean fields from quality-controlled monthly data. For each year, we then compute the zonal centroid from these annual fields, creating a centroid time series. The shift speed is the linear trend of this time series, with a positive value indicating a shoreward shift. Finally, the global average shift speed is the area-weighted average of the regional speeds.

EKE calculation

EKE is defined as the kinetic energy of oceanic mesoscale activities. The calculation formula of EKE is as follows:

$$EKE = \frac{1}{2} (\bar{u}^2 + \bar{v}^2) \quad (4)$$

where u' and v' are the zonal and meridional components of perturbation sea surface velocity, respectively, which are obtained by applying 150 km spatial high-pass filtering to the GLORYS, AVISO, CMEMS, OFES and CMIP6 data at their respective minimum temporal resolutions. The overbar denotes a spatial average over 150 km. Additionally, we tested several cutoff wavelengths of filtering, including 50 km, 100 km, and 200 km. The results are consistent with each other. 150 km is applied for all spatial filtering in the study.

|∇SST| calculation

|∇SST| is defined as the magnitude of ∇SST,

$$|\nabla S S T| = \sqrt{\left(\frac{\partial S S T'}{\partial x} \right)^2 + \left(\frac{\partial S S T'}{\partial y} \right)^2} \quad (5)$$

where SST' is the mesoscale sea surface temperature field, which is obtained by applying a 150 km high-pass filtering to OISST, GLORYS, OFES and CMIP6 sea surface temperature data at their minimum temporal resolution.

EKE source terms

We calculate the global trends of the primary source terms responsible for the temporal evolution of EKE, including surface wind power (WP), baroclinic energy conversion rates (BC), and barotropic energy

conversion rates (BT) from monthly GLORYS^{34,35}.

$$WP = \frac{1}{\rho_0} \tau_w \cdot u'_s \quad (6)$$

$$BT = - \left(u' \bar{v}' \frac{\partial \bar{u}}{\partial x} + u' v' \left(\frac{\partial \bar{u}}{\partial y} + \frac{\partial \bar{v}}{\partial x} \right) + v' \bar{v}' \frac{\partial \bar{v}}{\partial y} \right) \quad (7)$$

$$BC = - \frac{g}{\rho_0 \frac{dp}{dz}} \left(u' \bar{\rho}' \frac{\partial \bar{\rho}}{\partial x} + v' \bar{\rho}' \frac{\partial \bar{\rho}}{\partial y} \right) \quad (8)$$

where τ_w is the surface wind stress from ORASS and u'_s is the horizontal current at the sea surface. u and v are the components of the seawater velocity. Here, g is the acceleration of gravity, $\rho_0 = 1025 \text{ kg/m}^3$ is the reference density. The overbar (prime) represents the low-pass (high-pass) filter.

Significance test

In this study, a unary linear regression model $\hat{x} = \hat{\beta}_0 + \hat{\beta}T$ is used to analyze the linear trend of zonal centroids, where the superscript (hat) represents the estimated values. $\hat{\beta}$ is the estimate of the slope, $\hat{\beta}_0$ is the estimate of the intercept, \hat{x} and T represent the zonal centroid and time, respectively. The significance test for the linear trend (namely the slope $\hat{\beta}$) used in this study is based on the Student's t -test, where the used t -statistic is:

$$t = \frac{\hat{\beta} \sqrt{S_T}}{\hat{\sigma}} \quad (9)$$

$S_T = \sum_{i=1}^{n-2} (T_i - \hat{T})^2 \hat{x}$ and \hat{T} represent the estimated value of zonal centroid and time, respectively. n is the length of the time series. $\hat{\sigma}$ is the unbiased estimate of the residual standard deviation. If,

$$|t| > t_{\frac{\alpha}{2}}(n-2) \quad (10)$$

Then the trend is significant, else the trend is not significant. Where $t_{\frac{\alpha}{2}}(n-2)$ represents the upper $\frac{\alpha}{2}$ quantile of the t -distribution with an effective degree of freedom of $n-2$, α is the significance level, in this paper, $\alpha = 0.05, 0.1$. To eliminate heteroscedasticity and autocorrelation in each time series, we implemented the Newey-West heteroscedasticity and autocorrelation consistent (HAC) covariance matrix estimator to correct standard errors and adjust confidence intervals.

Data availability

The GLORYS data used in this study can be downloaded from https://data.marine.copernicus.eu/product/GLOBAL_MULTIYEAR_PHY_001_030 The OFES data can be downloaded from <https://www.jamstec.go.jp/esc/fes/dods/OFES>. The OISSTv2.1 data can be obtained from <https://www.ncei.noaa.gov/products/optimum-interpolation-sst>. The AVISO and CMEMS data can be downloaded from <https://www.aviso.altimetry.fr> and https://data.marine.copernicus.eu/product/SEALEVEL_GLO_PHY_L4_MY_008_047, respectively. The CMIP6 datasets used in this study were downloaded from <https://pcmdi.llnl.gov/CMIP6>. The ORASS data used for wind power calculation can be accessed from <https://cds.climate.copernicus.eu/datasets/reanalysis-oras5?tab=overview>.

Code availability

MATLAB codes to reproduce the analyses are available upon request from the corresponding author or can be accessed from <https://doi.org/10.5281/zenodo.17093765>.

References

- Ferrari, R. & Wunsch, C. Ocean circulation kinetic energy: reservoirs, sources, and sinks. *Annu. Rev. Fluid Mech.* **41**, 253–282 (2009).
- Chelton, D. B., Gaube, P., Schlax, M. G., Early, J. J. & Samelson, R. M. The influence of nonlinear mesoscale eddies on near-surface oceanic chlorophyll. *Science* **334**, 328–332 (2011).
- Dong, C., McWilliams, J. C., Liu, Y. & Chen, D. Global heat and salt transports by eddy movement. *Nat. Commun.* **5**, 3294 (2014).
- Zhang, Z., Wang, W. & Qiu, B. Oceanic mass transport by mesoscale eddies. *Science* **345**, 322–324 (2014).
- Xing, Q., Yu, H. & Wang, H. Global mapping and evolution of persistent fronts in Large Marine Ecosystems over the past 40 years. *Nat. Commun.* **15**, 4090 (2024).
- Gill, A., Green, J. & Simmons, A. in *Deep Sea Research and Oceanographic Abstracts*. Vol. 21, 499–528 (Elsevier, 1974).
- Couespel, D., Lévy, M. & Bopp, L. Stronger carbon uptake by the ocean in eddy-resolving simulations of global warming. *Geophys. Res. Lett.* **51**, e2023GL106172 (2024).
- Bian, C. et al. Oceanic mesoscale eddies as crucial drivers of global marine heatwaves. *Nat. Commun.* **14**, 2970 (2023).
- Wang, H., Qiu, B., Liu, H. & Zhang, Z. Doubling of surface oceanic meridional heat transport by non-symmetry of mesoscale eddies. *Nat. Commun.* **14**, 5460 (2023).
- Damien, P., Bianchi, D., Kessouri, F. & McWilliams, J. C. Modulation of phytoplankton uptake by mesoscale and submesoscale eddies in the California current system. *Geophys. Res. Lett.* **50**, e2023GL104853.
- Zhang, X. et al. Midlatitude mesoscale thermal air-sea interaction enhanced by greenhouse warming. *Nat. Commun.* **15**, 7699 (2024).
- Le, P. T., Hardesty, B. D., Auman, H. J. & Fischer, A. M. Frontal processes as drivers of floating marine debris in coastal areas. *Marine Environ. Res.* **200**, 106654 (2024).
- McGillicuddy, D. J. Jr. et al. Eddy/wind interactions stimulate extraordinary mid-ocean plankton blooms. *Science* **316**, 1021–1026 (2007).
- Currie, J. C. et al. A novel approach to assess distribution trends from fisheries survey data. *Fish. Res.* **214**, 98–109 (2019).
- Oliver, E. C., O’Kane, T. J. & Holbrook, N. J. Projected changes to Tasman Sea eddies in a future climate. *J. Geophys. Res. Oceans* **120**, 7150–7165 (2015).
- Johnson, G. C. & Lyman, J. M. Warming trends increasingly dominate global ocean. *Nat. Clim. Change* **10**, 757–761 (2020).
- Beech, N. et al. Long-term evolution of ocean eddy activity in a warming world. *Nat. Clim. Change* **12**, 910–917 (2022).
- Martínez-Moreno, J. et al. Global changes in oceanic mesoscale currents over the satellite altimetry record. *Nat. Clim. Change* **11**, 397–403 (2021).
- Li, J., Roughan, M. & Kerry, C. Drivers of ocean warming in the western boundary currents of the Southern Hemisphere. *Nat. Clim. Change* **12**, 901–909 (2022).
- Li, X. et al. Eddy activity in the Arctic Ocean projected to surge in a warming world. *Nat. Clim. Change* **14**, 156–162 (2024).
- Yang, H. Warming hotspots induced by more eddies. *Nat. Clim. Change* **12**, 889–890 (2022).
- Yun, J., Ha, K.-J. & Lee, S.-S. Impact of greenhouse warming on mesoscale eddy characteristics in high-resolution climate simulations. *Environ. Res. Lett.* **19**, 014078 (2024).
- Hogg, A. M. et al. Recent trends in the southern ocean eddy field. *J. Geophys. Res. Oceans* **120**, 257–267 (2015).
- Shi, F. et al. Contrasting trends in short-lived and long-lived mesoscale eddies in the Southern Ocean since the 1990s. *Environ. Res. Lett.* **18**, 034042 (2023).

25. Beal, L. M. & Elipot, S. Broadening not strengthening of the Agulhas Current since the early 1990s. *Nature* **540**, 570–573 (2016).
26. Todd, R. E. & Ren, A. S. Warming and lateral shift of the Gulf Stream from in situ observations since 2001. *Nat. Clim. Change* **13**, 1348–1352 (2023).
27. Eyring, V. et al. Overview of the Coupled Model Intercomparison Project Phase 6 (CMIP6) experimental design and organization. *Geosci. Model Dev.* **9**, 1937–1958 (2016).
28. Yang, H. et al. Poleward shift of the major ocean gyres detected in a warming climate. *Geophys. Res. Lett.* **47**, e2019GL085868 (2020).
29. McCoy, D., Bianchi, D. & Stewart, A. L. Global observations of sub-mesoscale coherent vortices in the ocean. *Prog. Oceanogr.* **189**, 102452 (2020).
30. Wu, L. et al. Enhanced warming over the global subtropical western boundary currents. *Nat. Clim. Change* **2**, 161–166 (2012).
31. Yang, H. et al. Intensification and poleward shift of subtropical western boundary currents in a warming climate. *J. Geophys. Res. Oceans* **121**, 4928–4945 (2016).
32. Burls, N. & Reason, C. Sea surface temperature fronts in the mid-latitude South Atlantic revealed by using microwave satellite data. *J. Geophys. Res. Oceans* **111**, C08001 (2006).
33. Goni, G. J., Bringas, F. & DiNezio, P. N. Observed low frequency variability of the Brazil Current front. *J. Geophys. Res. Oceans* **116**, <https://doi.org/10.1029/2011JC007198> (2011).
34. Wang, Q. & Tang, Y. The interannual variability of eddy kinetic energy in the Kuroshio large meander region and its relationship to the Kuroshio latitudinal position at 140 E. *J. Geophys. Res. Oceans* **127**, e2021JC017915 (2022).
35. Wang, S. et al. A more quiescent deep ocean under global warming. *Nat. Clim. Change* **14**, 961–967 (2024).
36. Renault, L. et al. Modulation of wind work by oceanic current interaction with the atmosphere. *J. Phys. Oceanogr.* **46**, 1685–1704 (2016).
37. Renault, L., Molemaker, M. J., Gula, J., Masson, S. & McWilliams, J. C. Control and stabilization of the Gulf Stream by oceanic current interaction with the atmosphere. *J. Phys. Oceanogr.* **46**, 3439–3453 (2016).
38. Rai, S., Hecht, M., Maltrud, M. & Aluie, H. Scale of oceanic eddy killing by wind from global satellite observations. *Sci. Adv.* **7**, eabf4920 (2021).
39. Yang, H. et al. Onshore intensification of subtropical western boundary currents in a warming climate. *Nat. Clim. Change* **15**, 301–307 (2025).
40. Sallée, J.-B. et al. Summertime increases in upper-ocean stratification and mixed-layer depth. *Nature* **591**, 592–598 (2021).
41. Guo, H., Cai, J., Yang, H. & Chen, Z. Observations reveal onshore acceleration and offshore deceleration of the Kuroshio Current in the East China Sea over the past three decades. *Environ. Res. Lett.* **19**, 024020 (2024).
42. Bakun, A. Global climate change and intensification of coastal ocean upwelling. *Science* **247**, 198–201 (1990).
43. Hewitt, H. T. et al. Resolving and parameterising the ocean mesoscale in Earth system models. *Curr. Clim. Change Rep.* **6**, 137–152 (2020).
44. Chelton, D. B., DeSzoeke, R. A., Schlax, M. G., El Naggar, K. & Siwertz, N. Geographical variability of the first baroclinic Rossby radius of deformation. *J. Phys. Oceanogr.* **28**, 433–460 (1998).
45. Lv, T. et al. The coastal front modulates the timing and magnitude of spring phytoplankton bloom in the Yellow Sea. *Water Res.* **220**, 118669 (2022).
46. Mahadevan, A. The impact of submesoscale physics on primary productivity of plankton. *Annu. Rev. Mar. Sci.* **8**, 161–184 (2016).
47. Zhao, D., Xu, Y., Zhang, X. & Huang, C. Global chlorophyll distribution induced by mesoscale eddies. *Remote Sens. Environ.* **254**, 112245 (2021).
48. Jin, P. et al. Eddy impacts on abundance and habitat distribution of a large predatory squid off Peru. *Mar. Environ. Res.* **195**, 106368 (2024).
49. Castillo-Trujillo, A. C. et al. An evaluation of eight global ocean reanalyses for the Northeast US continental shelf. *Prog. Oceanogr.* **219**, 103126 (2023).

Acknowledgements

The authors would like to thank Prof. Hu Yang, Prof. Yanluan Lin, and Prof. Jihai Dong for their helpful comments and suggestions. This research was funded by the National Key Research and Development Program of China (2021YFC3101601 to F.X.), and the National Natural Science Foundation of China (42176019 to F.X., 42476005 to H.L., and 424B2044 to S.Z.).

Author contributions

S.Z. and F.X. conceived the study. S.Z. and Y.Z. prepared the figures and wrote the manuscript. H.L., L.L., E.L., and F.X. contributed to interpreting the results and improving the manuscript.

Competing interests

The authors declare no competing interests.

Additional information

Supplementary information The online version contains supplementary material available at <https://doi.org/10.1038/s41467-025-65359-x>.

Correspondence and requests for materials should be addressed to Fanghua Xu.

Peer review information *Nature Communications* thanks Zhiwei Zhang and the other, anonymous, reviewers for their contribution to the peer review of this work. A peer review file is available.

Reprints and permissions information is available at <http://www.nature.com/reprints>

Publisher's note Springer Nature remains neutral with regard to jurisdictional claims in published maps and institutional affiliations.

Open Access This article is licensed under a Creative Commons Attribution-NonCommercial-NoDerivatives 4.0 International License, which permits any non-commercial use, sharing, distribution and reproduction in any medium or format, as long as you give appropriate credit to the original author(s) and the source, provide a link to the Creative Commons licence, and indicate if you modified the licensed material. You do not have permission under this licence to share adapted material derived from this article or parts of it. The images or other third party material in this article are included in the article's Creative Commons licence, unless indicated otherwise in a credit line to the material. If material is not included in the article's Creative Commons licence and your intended use is not permitted by statutory regulation or exceeds the permitted use, you will need to obtain permission directly from the copyright holder. To view a copy of this licence, visit <http://creativecommons.org/licenses/by-nc-nd/4.0/>.

© The Author(s) 2025